Journal of Modern Optics
Vol. 57, No. 18, 20 October 2010, 1759–1769

Taylor & Francis
Taylor & Francis Group

Active infrared thermography applied to defect detection and characterization on asphalt pavement samples: comparison between experiments and numerical simulations

J. Dumoulin[a]*, L. Ibos[b], C. Ibarra-Castanedo[c], A. Mazioud[b], M. Marchetti[d], X. Maldague[c] and A. Bendada[c]

[a]*Université Paris-Est, Laboratoire Central des Ponts et Chaussées (LCPC), Bouguenais, France;* [b]*Université Paris-Est, CERTES, Créteil, France;* [c]*Computer Vision and Systems Laboratory, Laval University, Quebec (PQ) Canada;* [d]*Regional Laboratory of Nancy, CETE de l'Est, Tomblaine, France*

(*Received 5 January 2010; final version received 6 September 2010*)

This work is devoted to the application of active infrared thermography to defect detection in pavement structures. The challenge is to localize and to determine some properties of defects (e.g. shape and depth) into a highly heterogeneous material. Experimental work was carried out in laboratory conditions using a pavement sample containing two defects (wood and air). Pulsed thermography results were compared with FLUENT numerical simulations. Different preliminary approaches were investigated to analyze data: singular value decomposition of infrared image sequences, contrast image methods and computation of thermal effusivity considering a heat transfer model in a semi-infinite material. This last method is more sensitive to experimental conditions such as the presence of natural convection at a sample surface. However, all methods allow detection of one defect into the pavement sample.

Keywords: active infrared thermography; non-destructive testing; bitumen concrete; heat transfer

1. Introduction

In many countries, the road network is aging while road traffic and maintenance costs are increasing. Nowadays, thousands and thousands of kilometres of roads are submitted to surface distress surveys each year. These surveys generally use pavement surface imaging measurement techniques [1], mainly in the visible spectrum, coupled with visual inspection or image processing detection of emergent distresses [2]. Nevertheless, optimization of maintenance works and costs require an early detection of defects inside the pavement structure when they are still hidden under the surface.

Accordingly, alternative measurement techniques for the non-destructive testing (NDT) of pavement are currently under investigation [3,4]. In this context, NDT by active infrared thermography could be a complementary full field approach.

Active infrared thermography for the detection of defects has been used for many years now for the non-destructive control of materials such as metals, composites and so on, as described in the literature [5]. Its application to civil engineering materials, such as cement concrete, a slightly porous and almost homogeneous material, was shown in [6]. A first extension of such an approach for bitumen concrete material was presented in [7], where the challenge was to sort the relevant signals of defects from the pristine porosity and heterogeneity of such a material.

In this paper, pulsed thermography (PT) and principal component thermography (PCT) analysis were conducted, both on experimental and numerical experimentations, as a preliminary study. They were applied to a heterogeneous asphalt concrete pavement sample having two defect geometries of different natures. Two methods were used to retrieve the depth of the defects, and the results obtained are discussed and analyzed. Finally, combining numerical simulations with experiments allowed us to discuss the influence of the sensitivity of the uncooled IR detector used in the potential detection of subsurface defects.

2. Context and objectives

Pavement distress is essentially due to heavy vehicle traffic and adverse weather conditions. Indeed, defects such as unsticking zones between the top layer (wearing course) and the structural ones (Figure 1) could induce a quick deterioration of the pavement surface (circular cracking up to potholes).

*Corresponding author. Email: jean.dumoulin@lcpc.fr

ISSN 0950–0340 print/ISSN 1362–3044 online

DOI: 10.1080/09500340.2010.522738
http://www.informaworld.com

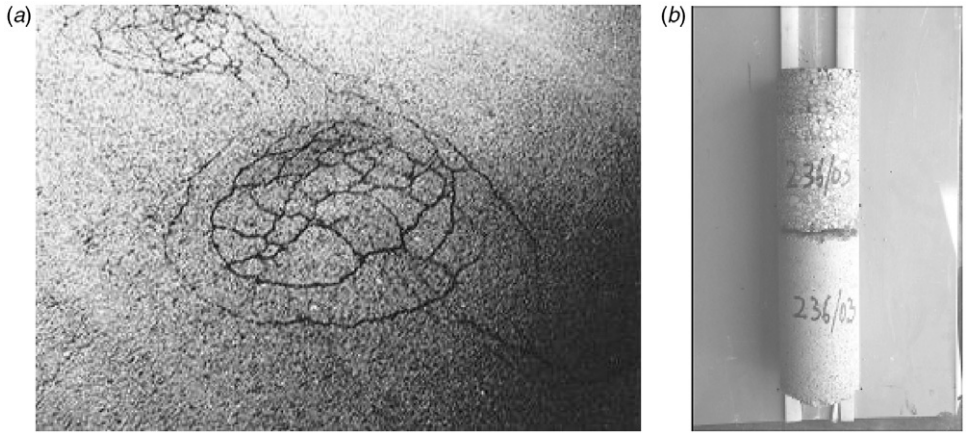

Figure 1. Local pavement surface emergent cracking (left) probably due to debonding (right).

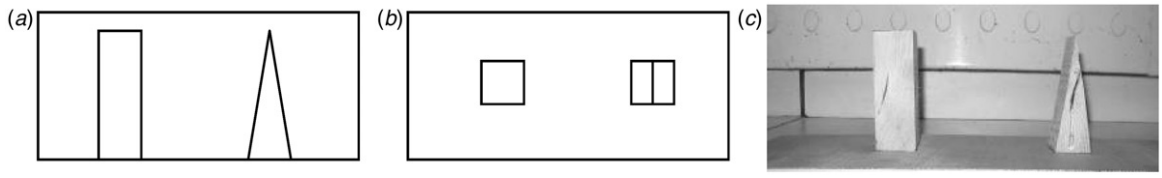

Figure 2. (*a*) Side view, (*b*) top view, (*c*) and defects installed on a wood slab (removed during experiments).

Figure 1(*b*) shows a core of pavement structure with a debonding between the base and the subbase layers of the pavement structure. The same problem (not illustrated here) could occur between the pavement surface course and the base layer and then induce stripping of materials from the road surface.

Furthermore, there is an extremely large variety of materials used for road construction, from asphalt to cement concrete. These have different granular constitutions and therefore different thermal and radiative (reflective/absorbing) properties. The porosity of these structures varies from non-porous to highly porous. These variations could also appear within the same pavement layer due to construction constraints and/or bad implementation. Such inhomogeneity would then induce additional difficulties in the use of active thermography.

In the present study, semi-granular asphalt pavement materials were considered. Their nature was of the most commonly used material on French national roads. Two parallelepiped samples (10 cm × 18 cm × 50 cm) were fabricated using granular materials with a bitumen matrix. Two defects made of Pine wood (a parallelepiped and a pyramid) were included while manufacturing the road samples (Figure 2).

The pyramidal defect was chosen as it partly matches the shape of a non-emergent crack. Pavement crack monitoring is actually done for an emergent crack using visual inspection on a real site or on the pavement surface images combined with image processing techniques to facilitate the pavement distress analysis process. Nevertheless, early pavement distress detection is required to minimize as much as possible the cost of pavement structure rehabilitation.

During the thermal analysis, these defects were either left in (i.e. wood defect) or removed from (i.e. air defect) the sample. Two kinds of inclusions were therefore evaluated, for which thermal conductivity (k) and effusivity ($b = \sqrt{k\rho C_p}$), wood or air, were lower than the ones for the road material. The upper parts of the defects were located 1.3 cm below the inspected sample surface. These inclusions were inserted into the road pavement samples in such a way that they did not thermally interact with each other (see Figure 3).

3. Square heating test bench

The experimental setup (Figure 4) was previously described in [7,8]. The road pavement sample is heated with two halogen lamps of 500 W each and inserted between two masonry blocks made of Syporex (to reduce lateral thermal dissipation).

A reflector was used to obtain a quasi-constant heat flux density over the whole sample surface. The selected active thermography method was the square

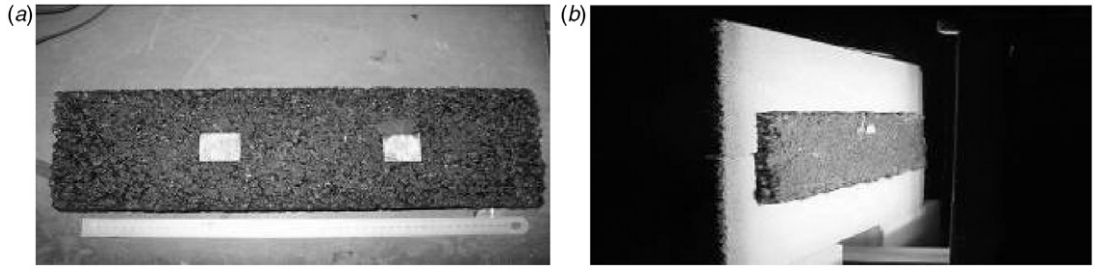

Figure 3. Pavement sample rear (*a*) and front (*b*) sides.

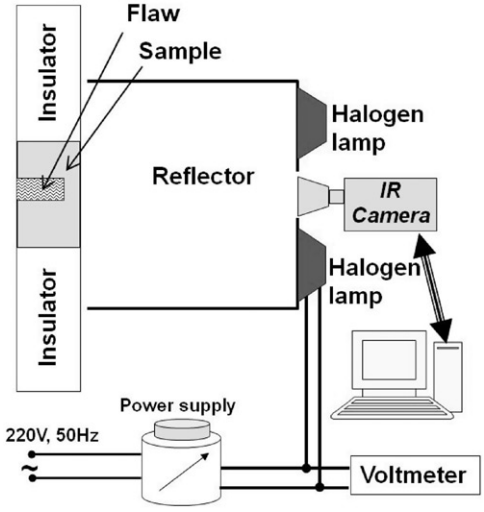

Figure 4. Scheme of the square heating test bench.

heating. The heating phase durations were of 60 s and 300 s. The heat flux density of the excitation during trials was assumed to be constant and around $3000\,\mathrm{W\,m^{-2}}$. The infrared camera was located at a distance of 0.8 m from the sample surface. A FLIR S65 infrared camera equipped with an uncooled microbolometer (FPA detector of 320×240 sensitive elements, spectral bandwidth 7.5–13 μm) was used.

An illustration of measurement results is plotted in Figure 5 for different areas, matching sound or defective parts of the studied pavement road sample. Both experimental thermograms obtained for 60 s and 300 s square heating show artifacts due to auto non-uniformity correction (NUC) operation at infrared camera level during measurements.

The deeper the defects, the harder their detection. There are two ways to improve detection. Either the level of heat flux is increased for the same pulse duration, or a longer heat pulse is used. In the second case, some difficulties will appear due to heat losses and 3D internal conduction, which will ultimately blur thermal images. The work presented below is a preliminary approach, where a square heating method was used along with several data analysis techniques. Although the heat pulses provided by the halogen lamps are actually closer to square pulses, the data treatments were based on the assumption of a Dirac pulse excitation as a first approximation. In addition, a square pulse heat transfer solution for a semi-infinite body was developed.

4. Numerical simulation

In parallel to these experimental trials and for a similar heat density pulse and thermal relaxation duration, numerical simulations based on the finite volume method of heat transfer inside the investigated sample were carried out using FLUENT.

The modeling part consisted of applying a square function of $2620\,\mathrm{W\,m^{-2}}$ heat flux density for two pulse durations (60 s and 300 s) to the front face of the sample. For these numerical test cases, the temperature fields as a function of time on the surface and inside the sample were computed. The geometry of the considered sample matches the two defect configurations. According to this geometry, we used a three-dimensional non-structured meshing based on 1,892,429 tetrahedral cells realized under GAMBIT.

The thermal characteristics of the materials used in the numerical simulations are presented in Table 1.

Furthermore, ambient temperature was considered as constant (equal to 20°C), and the sample was supposed to be submitted to a global convective heat exchange coefficient $h = 10\,\mathrm{W\,m^{-2}K^{-1}}$, on its front and rear faces. Lateral faces were insulated.

An illustration of numerical simulation results is provided in Figure 6 for heat pulse durations equivalent those shown in Figure 5.

Thermograms extracted from 3D numerical simulations are not affected by noise, and the pavement sample is supposed to have homogeneous thermal behavior, which is not the case for real samples.

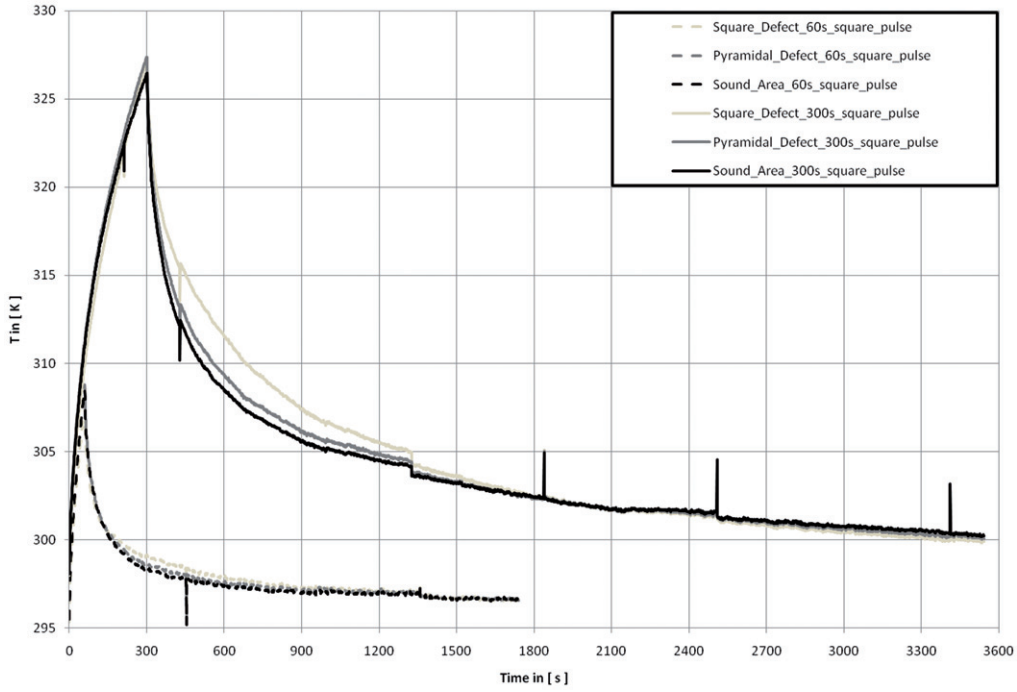

Figure 5. Temperature evolution during trials for 60 s and 300 s square heating durations with defects in pine wood. (The color version of this figure is included in the online version of the journal.)

Table 1. Thermal and physical properties of materials used for numerical simulations.

Material	k ($\mathrm{W\,m^{-1}\,K^{-1}}$)	ρ ($\mathrm{kg\,m^{-3}}$)	Cp ($\mathrm{J\,kg^{-1}\,K^{-1}}$)
Asphalt	1.41	2262	1255
Pine wood	0.15	600	1900
Air	0.024	1.225	1006
Water	0.6	998.2	4182

5. Defect detection by singular value decomposition

Singular value decomposition (SVD) is an interesting tool for the extraction of the spatial and temporal information from a thermographic matrix in a compact or simplified manner. Instead of relying on a basis function (such as in pulsed phase thermography, which is based on the Fourier transform relying on sinusoidal basis functions), SVD is an eigenvector-based transform that forms an orthonormal space. SVD is close to principal component analysis (PCA) but SVD simultaneously provides the PCAs in both row and column spaces.

The SVD of an $M \times N$ matrix $\mathbf{A}$ ($M > N$) can be calculated as follows [9]:

$$\mathbf{A} = \mathbf{USV}^{\mathrm{T}} \tag{1}$$

where $\mathbf{U}$ is an $\mathrm{M} \times \mathrm{N}$ orthogonal matrix, $\mathbf{S}$ being a diagonal $N \times N$ matrix (with the singular values of $\mathbf{A}$ in the diagonal), and $\mathbf{V}^{\mathrm{T}}$ is the transpose of an $\mathrm{N} \times \mathrm{N}$ orthogonal matrix (characteristic time).

Hence, to apply the SVD to thermographic data, the 3D thermogram matrix representing time and spatial variations has to be reorganized as a 2D $M \times N$ matrix $\mathbf{A}$ as depicted in Figure 7. This can be done by rearranging the thermograms for each time step as columns in $\mathbf{A}$, in such a way that time variations will occur column-wise while spatial variations will occur row-wise.

Under this configuration, the columns of $\mathbf{U}$ represent a set of orthogonal statistical modes known as empirical orthogonal functions (EOF) that describe the spatial variations of data [10,11]. On the other hand, the principal components (PCs), which represent time variations, are arranged row-wise in matrix $\mathbf{V}^{\mathrm{T}}$. The first EOF will represent the most characteristic variability of the data; the second EOF will contain the second most important variability, and so on. Usually, original data can be adequately represented with only a few EOFs. Typically, a sequence of 1000 thermal images can be replaced by 10 or fewer EOFs.

In Figure 8 an illustration of SVD is shown for simulated and experimental data obtained for two pine wood defects inserted in a pavement sample.

It is noticeable from these images that the parallelepiped defect is easily detected in both simulated and experimental data. The pyramid defect, on the other

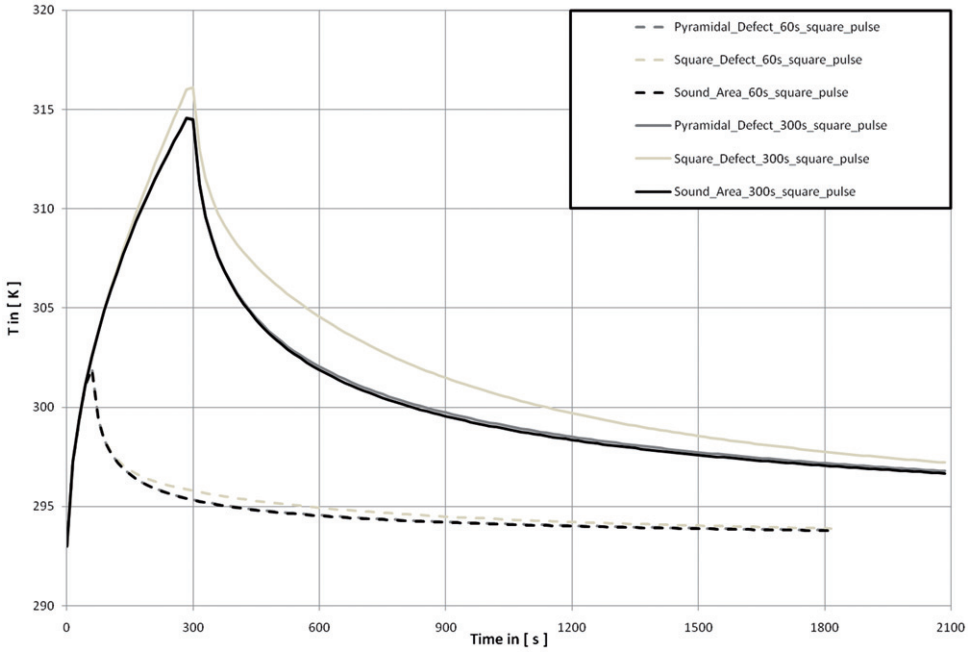

Figure 6. Thermograms extracted from 3D numerical simulations for 60 s and 300 s square heating durations with defects in pine wood. (The color version of this figure is included in the online version of the journal.)

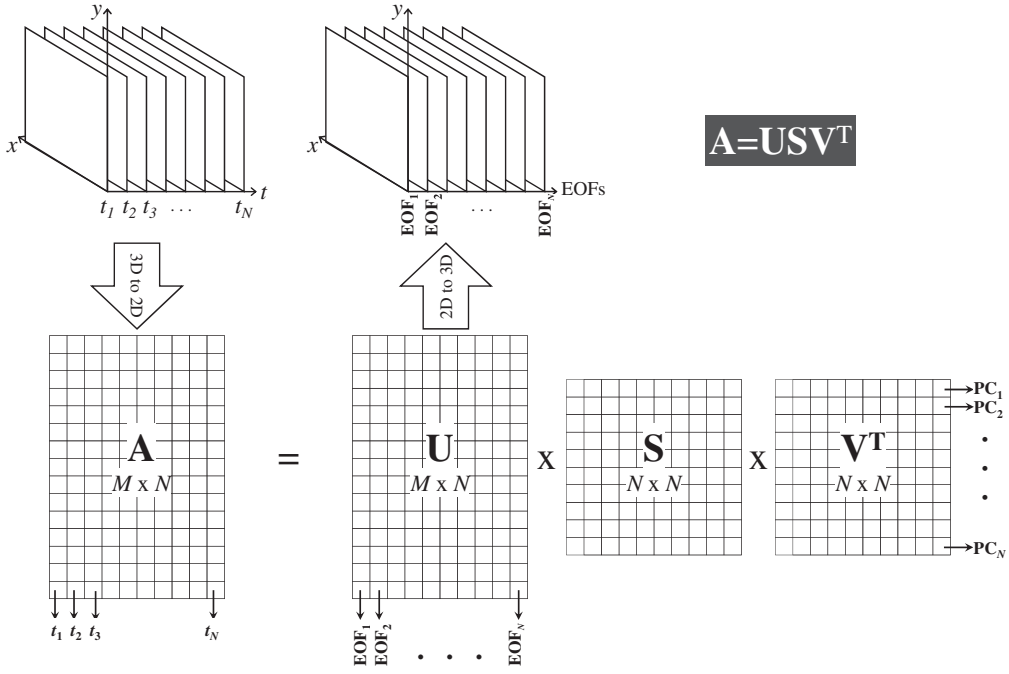

Figure 7. Schematic representation of the application of the SVD to thermographic data.

hand, requires further data analysis to be detected. Experimental data are extremely affected by natural convection and noise induced by aggregate thermal behavior during the heating and relaxation phases. Hence, the pyramid defect was only detected using simulated data.

6. Defect depth characterization on thermal image sequence

Two preliminary approaches are presented in this section. The first uses the localization of the defect with the SVD method presented in previous section and a correlation proposed in literature. The second

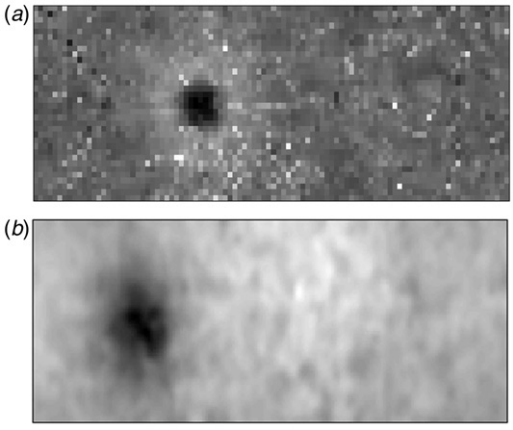

Figure 8. EOF map computed: simulated (*a*) – experimental (*b*) with detection of parallelepiped defect for a 300 s square heating.

approach does not require a first localization of the defect to determine the depth.

6.1. Maximum contrast approach

Thermal contrast is a basic operation that, despite its simplicity, is at the origin of many PT algorithms. Numerous thermal contrast definitions exist but they all share the need for specifying a sound area, Sa, i.e. a defect-free region within the region of interest. For instance, the absolute thermal contrast Ct_{abs} and the running contrast Ct_{run} are defined as [5]:

$$Ct_{\mathrm{abs}} = \Delta T(t) = T_d(t) - T_{\mathrm{Sa}}(t) \text{ and } Ct_{\mathrm{run}} = \frac{T_d(t) - T_{\mathrm{Sa}}(t)}{T_{\mathrm{S_a}}(t)} \tag{2}$$

with $T_d(t)$ the temperature of a pixel or the average value of a group of pixels on a defective area at time t, and $T_{\mathrm{Sa}}(t)$ the temperature at time t over a sound area (Sa) on a pixel or for the average value of a group of pixels.

It is also possible to use the standard contrast (see [5]) as presented in the following expression (3).

$$Ct_{\mathrm{std}} = \frac{T_d(t) - T_d(0)}{T_{\mathrm{Sa}}(t) - T_{\mathrm{S_a}}(0)}. \tag{3}$$

But care has to be taken with the behavior of this inhomogeneous material during the heating phase. Bitumen binder and aggregates do not have the same diffusive thermal time constant (see Figure 9). Such phenomenon vanishes with the establishment of the 3D heat diffusion according to the spatial resolution used for infrared measurements (see Figure 9). Therefore, the standard contrast formula has to be modified by substituting T_{Sa} by at least the average of the sound area values. For instance, the sound area can be determined by labeling the EOF map obtained by SVD (as presented in the previous paragraph) or by using the average of the whole thermal image, assuming that defect size is negligible versus the sound area [7]. Nevertheless, in this paper, only absolute and running contrasts are considered.

Although this approach was established for pulse heating thermography applied for flaw detection in carbon epoxy specimens or carbon fiber reinforced plastic (CFRP) plate bonded on a concrete structure, we have evaluated the possibility of computing the defect depth z by extracting a few parameters on the thermal contrast curve, such as the maximum contrast $\Delta T_{\max}$ and its time of occurrence $t_{\max}$ using the thermal diffusion time concept and the hypothesis of heat diffusion in a semi-infinite body [12,13]. Time associated with the maximum contrast can be linked to the defect depth and thermal diffusivity of the studied material as follows:

$$z = \sqrt{t_{\max} a} \tag{4}$$

where a is the thermal diffusivity of the material, $t_{\max}$ the maximum contrast time and z the calculated depth.

As we use a square heating excitation and not a pulse, a first-order correction consisting of moving the time scale origin towards the square heating duration barycentre was made, as suggested by Degiovanni [14].

Figure 10 shows the temperature excess evolution for experiments and numerical simulations for the 60 s and 300 s square heat durations. The sound and defect thermograms were established by averaging the temperature in a rectangular area at each time step. Localization of these areas was made using the SVD approach. The decimal logarithm was used for these log-log representations. The time origin is taken at the time of the energetic barycentre of the square heating.

The results for depth estimation and the time of maximum contrast presented hereafter (see Table 2) were obtained by using absolute contrast. During laboratory experiments, samples were at the thermal equilibrium before each test. Furthermore, the same hypothesis was achieved for numerical simulation.

In Table 2, depth estimation and time of the maximum contrast for two square pulse durations of 60 and 300 seconds are presented using the thermal diffusion time concept applied to experimental and simulated data.

These values were computed for the parallelepiped defect in pine wood.

Except for the 60 s experimental data, the depth estimated by this direct approach was in a good agreement with the geometry of the square defect inserted in the bitumen concrete sample. With such an approach, special care must be taken when choosing

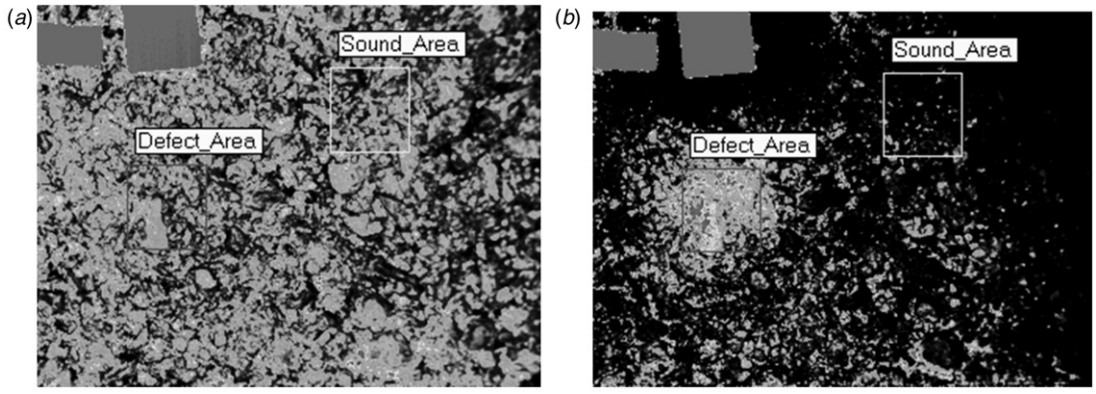

Figure 9. Thermal images at the end of a 60 s square heating (*a*) and 140 s after the end of heating (*b*) obtained with CEDIP Jade 3 cooled camera.

the sound area on thermal images, in particular with experimental data.

6.2. *Direct calculation on thermal image sequence: thermal model used*

Here, we assumed that the location of the defect was not known and we computed temperature excess maps through time using the temperature map acquired before the square heating at t_0 for each pixel (Equation (5)). This is a classical approach in wall heat transfer determination by IR thermography [15]. It is also quoted as cold image subtraction [5]:

$$\Delta T_{x,y}(t) = T_{x,y}(t) - T_{x,y}(t_0). \tag{5}$$

As a first approximation, heat transfer in pavement materials can be assumed to behave as a semi-infinite body. Nevertheless, care must be taken when choosing a time interval for the calculation and experiments (according to the material's characteristic thermal diffusion time), in order to preserve the validity of such a model. Furthermore, by neglecting natural heat transfer on the surface of the inspected material, the heat equation system to solve takes the following form:

$$\begin{cases} \frac{\partial^2\theta}{\partial z^2} = \frac{1}{a}\frac{\partial\theta}{\partial t} \text{ with } \theta(z,t) = T(z,t) - T_0 \\ \text{Initial condition:} \\ t \le 0\text{: } \theta\,(z,t) = 0 \\ \text{Boundary condition:} \\ t > 0 \text{ and } z = 0\text{: } -k\frac{\partial\theta}{\partial z} = \varphi_0(t). \end{cases} \tag{6}$$

In our measurement and simulation configuration, the surface solicitation is a constant square heat pulse of duration τ. The boundary condition at $t > 0$, Equation (6), takes the following expression where φ is the constant heat flux density applied during the pulse:

$$\varphi_0(t) = q_0 \text{ if } t \le \tau \text{ and } \varphi_0(t) = 0 \text{ if } t > \tau. \tag{7}$$

The solution of such a system can be obtained by using the Laplace transform. Other approaches can be found in the literature. For instance Vavilov in [16] presents different solutions for various thermal configurations. The solution for the surface temperature excess is:

$$\begin{cases} \text{if } t < \tau : \theta(0,t) = \frac{2q_0\sqrt{t}}{b\sqrt{\pi}} \\ \text{if } t \ge \tau : \theta(0,t) = \frac{2q_0}{b\sqrt{\pi}}\left(\sqrt{t} - \sqrt{t-\tau}\right) \end{cases} \tag{8}$$

where b is the sample thermal effusivity.

Combining this solution for the case of a square pulse solicitation over the surface of the studied material with the effusivity approach proposed by Balageas in [17] the depth of the defect can be determined using the relation:

$$z_{\text{def}} = \sqrt{a}\sqrt{t_{\min}}\left(b_{n,\min}\right)^{0.95} \tag{9}$$

where a is the thermal diffusivity, b the thermal effusivity, $t_{\min}$ the time when the effusivity curve is minimum, z_{def} the depth of the defect in m and $b_{n,\min}$ the normalized minimum effusivity $b_n = \frac{b}{b_{\text{Asphalt}}}$.

Thermal effusivity evolution for a square heat flux density pulse is obtained using Equation (9) and takes the expression reported in Equation (10).

$$\begin{cases} \text{if } t < \tau \quad b(t) = \frac{2q_0\sqrt{t}}{\theta(0,t)\sqrt{\pi}} \\ \text{if } t \ge \tau \quad b(t) = \frac{2q_0}{\theta(0,t)\sqrt{\pi}}\left(\sqrt{t} - \sqrt{t-\tau}\right). \end{cases} \tag{10}$$

Figure 11 presents the results obtained with simulated and measurement data matching the square heating case of 60 s and for pine wood defects. The depth obtained for the parallelepiped defect is in the range of 1.2 to 1.3 cm for numerical data and 1.1 to 1.4 cm for experimental data. In the case of experimental data, however, rear surface aggregates in the bitumen concrete locally degrade the homogeneity of depth in the spatial area that matches the defect.

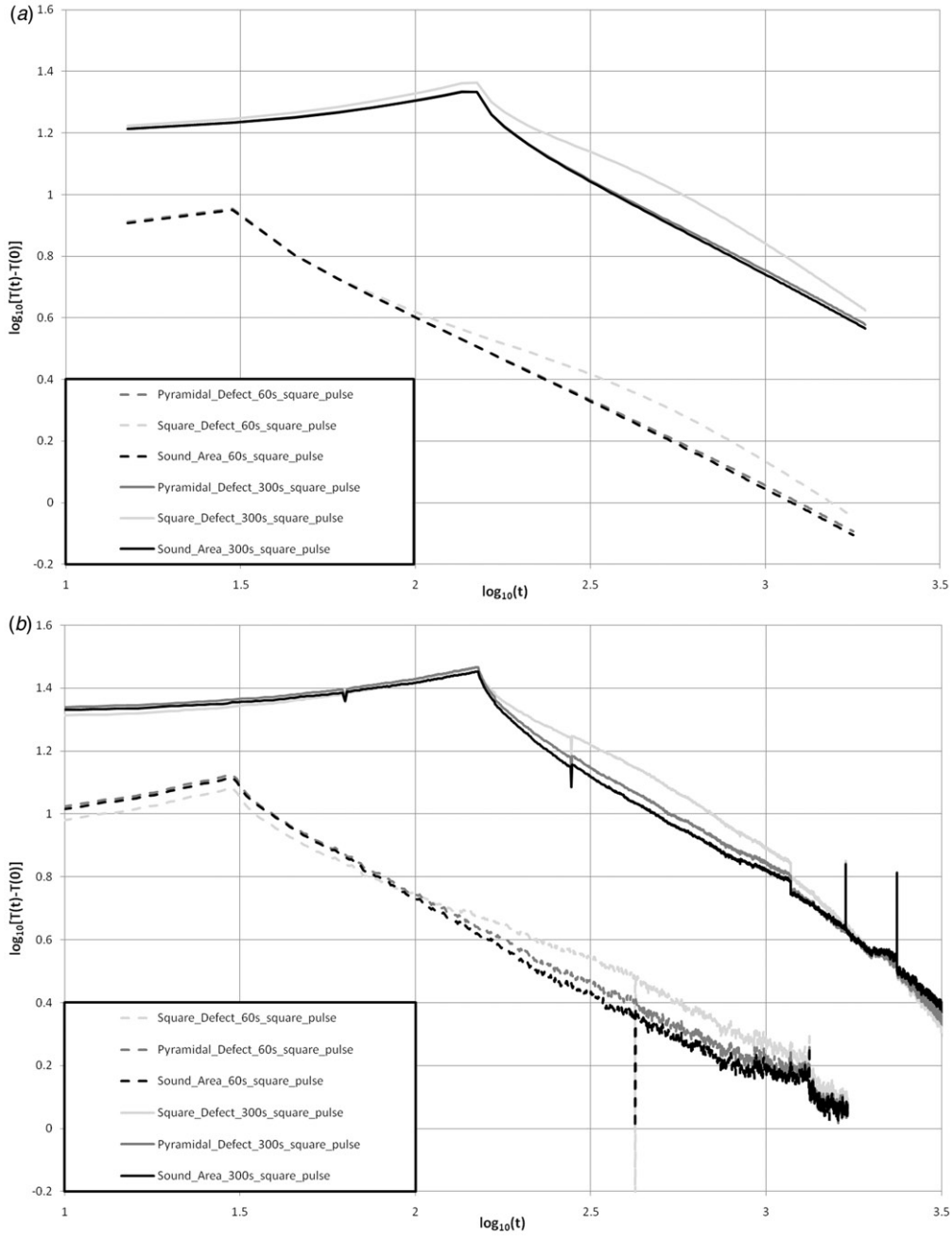

Figure 10. Decimal logarithmic representation of temperature excess over sound and defective (pine wood) areas: simulated (*a*) – experimental (*b*); square heating durations of 60 s and 300 s. (The color version of this figure is included in the online version of the journal.)

Table 2. Computed depth using thermal diffusion time concept and absolute contrast.

	Numerical simulations		Experimental data	
Square pulse duration	Time of maximum contrast in s	Estimated depth in mm	Time of maximum contrast in s	Estimated depth in mm
60 s	330	12.8	281	11.8
300 s	360	13.4	327	12.7

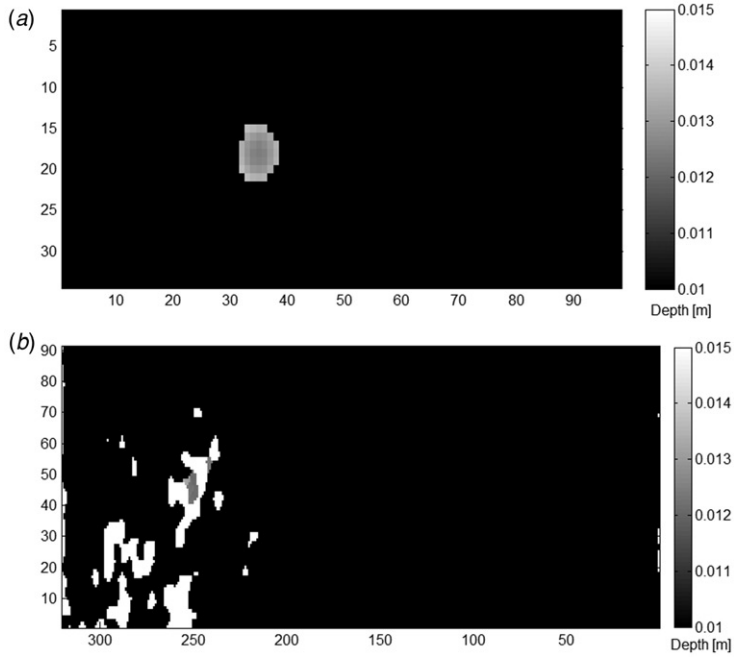

Figure 11. Square defect calculated depth maps in m: simulated (*a*) – experimental (*b*); heating duration of 60 s.

The natural convection phenomena observed in the experimental data coupled with the limited performances of the uncooled camera used in the experiments creates a more heterogeneous depth map. As expected, the direct calculation approach is more sensitive to these perturbations than an inverse approach using a regularization scheme. Here, the principal component thermography analysis presented in the previous section was helpful in analysing such a map.

Although the main interest of such an approach is to establish a map of the computed depths, it is also possible to perform a segmentation to obtain, simultaneously, the defect localization and one of its dimensional characteristics.

The influence of the defect composition is shown in Figure 12 using numerical simulation to retrieve the defect's depths using the thermal model. Furthermore, the influence of the square heating duration is also shown for a 60 s and 300 s pulses.

Some trends can be observed from the simulation results in Figure 12. For instance, in the case of water defects, the square heating pulse duration has to be increased in order to allow the detection, which is consistent given that the heat capacity of water is more than twice that of wood (see Table 1). In the case of air defects, results are similar for the two analyzed square heating pulses (60 and 300 s). No significant defect contrast improvement was observed for longer square heating excitation. For the pine wood defects, as can be seen from Figures 12 (300 s) and 11 (60 s), this defect is perfectly visible and the depth estimation results are of the correct order of magnitude, i.e. 1.3 cm. Furthermore, no significant defect contrast improvement is observed for longer excitation.

Finally, an interesting complementary study would be to vary the heat flux density intensity for the same duration.

7. Conclusion

Some preliminary pulsed thermography processing approaches, such as singular value decomposition on infrared images sequences, thermal contrast methods and computation of thermal effusivity considering a heat transfer model in a semi-infinite material, were considered for the detection of hidden fabricated defects (a parallelepiped and a pyramid) in an asphalt concrete material. The parallelepiped defect located at 1.3 cm under the surface was detected even with a short heating phase (test were made down to 60 s). The thermal behavior of the structure was greatly affected by the defect presence around it. The nature of the samples (porosity, heterogeneity) locally affected the ability of the technique for non-destructive control of such road material (through rear surface aggregate thermal behaviors). Furthermore, the natural convection thermal signature observed during experiments hid part of the defect's signal, in particular the pyramid defect. The semi-infinite model with the constant heat

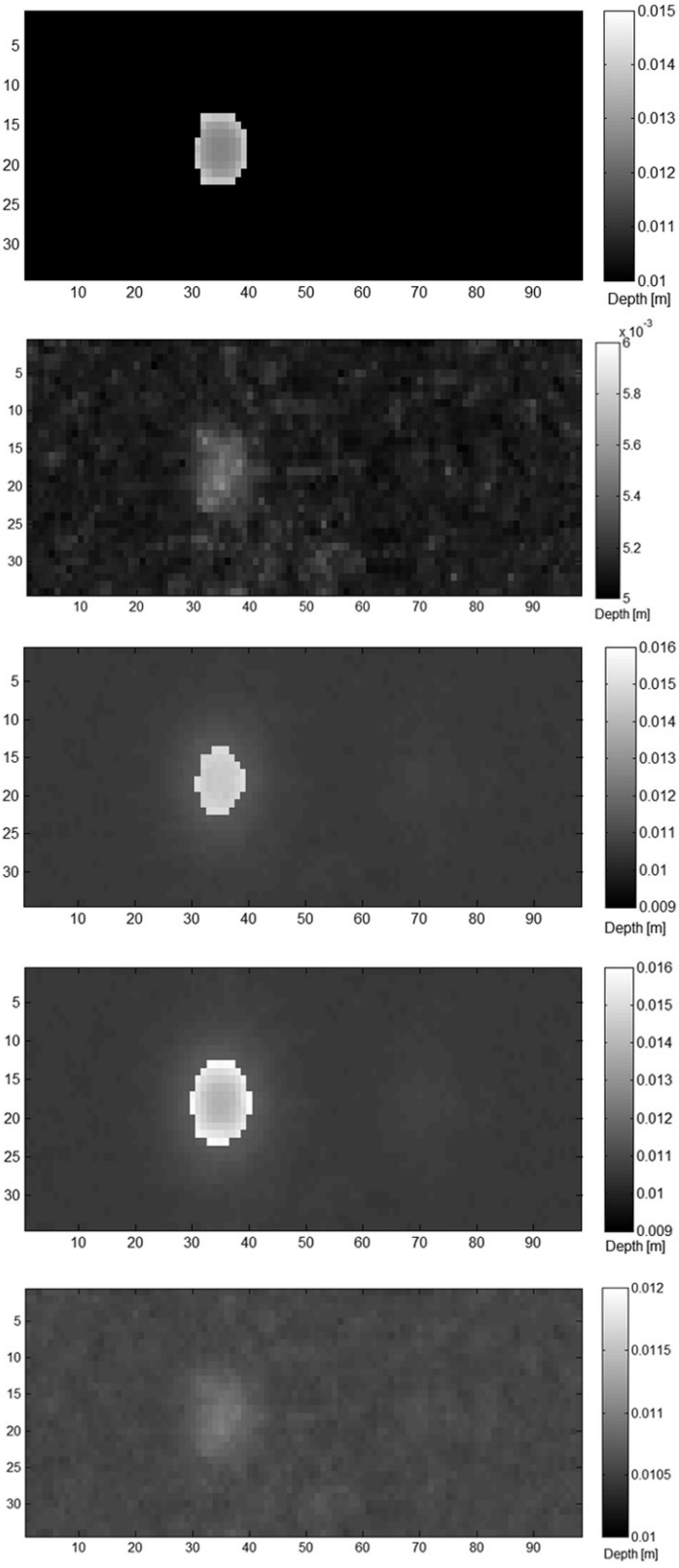

Figure 12. Square defect depth characterization versus defect type for two heat flux square pulse durations using simulated data.

pulse solution coupled with the normalized effusivity approach suggested by Balageas enabled the estimation of the parallelepiped defect depth. On the other hand, it was not possible to retrieve the depth information of the pyramid defect, not even using numerical simulations. Nevertheless, the use of principal component thermography has been shown to be very useful for fast defect detection and location, using its spatial signature on an empirical orthogonal functions map, especially for the pyramid defect. Finally, this study has also shown that it is possible to use uncooled infrared cameras with less thermal sensitivity to detect defects. Special care must be taken however for the reduction of measurement noise. This approach could be compared with the step heating one developed by Osiander et al. [18].

References

[1] Schmidt, B. Automated Pavement Cracking Assessment Equipment: State of the Art; Routes-Roads, World Road Association (PIARC), No. 320, October 2003, 35–44.

[2] Chambon, S.; Subirats, P.; Dumoulin, J. *Proceedings of IS&T/SPIE Electronic Imaging 2009: Machine Vision Applications*, San Jose, USA, Jan 21–22, 2009.

[3] Simonin, J-M.; Abraham, O. *Proceedings of the 6th International Symposium on NDT in Civil Engineering*, Al-Qadi, I., Washer, G., Eds, 14–18 August 2006, St Louis, MI, USA, 454–462.

[4] Fauchard, C.; Rejiba, F.; Dérobert, X.; Côte, Ph.; Sagnard, F. Step Frequency Radar Applied for Asphalt Thickness Measurements with Various Interface Conditions. *Proceedings of the 12th International Conference on Ground Penetrating Radar*, Birmingham, UK, June 16–18, 2008.

[5] Maldague, X.P.V. *Theory and Practice of Infrared Technology for Non-Destructive Testing*; Wiley: New York, 2001.

[6] Maierhofer, Ch.; Arndt, R.; Röllig, M.; Rieck, C.; Walther, A.; Scheel, H.; Hillemeier, B. *J. Cem. Conc. Compos.* **2006,** *28,* 393–401.

[7] Marchetti, M.; Ludwig, S.; Dumoulin, J.; Ibos, L.; Mazioud, A. Active Infrared Thermography for Non-destructive Control for Detection of Defects in Asphalt Pavements. *Proceedings of QIRT 2008 (Quantitative Infrared Thermography)*, Krakow, Poland, July 2–5, 2008.

[8] Larbi Youcef, M.; Mazioud, A.; Ibos, L.; Candau, Y.; Brémond, P.; Piro, M.; Filloux, A. A Non-destructive Method for Diagnostic of Insulated Building Walls Using Infrared Thermography. *Proceedings of Thermosense XXIX*, Orlando, USA, April 9–13, 2007.

[9] Rajic, N. *Compos. Struct.* **2002,** *58,* 521–528.

[10] Ibarra-Castanedo, C.; Gonzalez, D.A.; Galmiche, F.; Bendada, A.; Maldague, X. *Rec. Res. Dev. Appl. Phys.* **2006,** *9,* 101–127.

[11] Marinetti, S.; Grinzato, E.; Bison, P.G.; Bozzi, E.; Chimenti, M.; Pieri, G.; Salvetti, O. *Infrared Phys. Technol.* **2004,** *46(1–2),* 85–91.

[12] Ibarra-Castanedo, C.; González, D.; Klein, M.; Pilla, M.; Vallerand, S.; Maldague, X. *Infrared Phys.* **2004,** *46,* 75–83.

[13] Dumoulin, J.; Taillade, F.; Aubagnac, Ch.; Benzarti, K.; Quiertant, M. *The French Technology of Concrete – Special Issue for the Third International FIB Congress*, June 2010, 66–67 and on CD-Rom, 371–380.

[14] Degiovanni, A. *Int. J. Heat Mass Transfer* **1987,** *30,* 2199–2200.

[15] Dumoulin, J.; Millan, P.; Plazanet, M. *J. Flow Visual. Image Process.* **1995,** *2,* 219–236.

[16] Vavilov, V. Transient Thermal NDT: Conception in Formulae. *Proceedings of QIRT 92*, Paris, 1992.

[17] Balageas, D.L.; Deom, A.A.; Boscher, D.M. *J. Mat. Eval.* **1987,** *45,* 465–466.

[18] Osandier, R.; Spiecer, J.W.M. *Int. J. Heat Mass Transfer* **1998,** *37,* 680–692.